Resolving a ramp-flat structure from combined analysis of co- and post-seismic geodetic data: an example of the 2015 Pishan M_w 6.5 earthquake

Xiong Zhao,[1,2] Yangmao Wen [ORCID],[1,3,4] Caijun Xu [ORCID],[1,3,4] Kefeng He[1] and Torsten Dahm[2,5]

[1]*School of Geodesy and Geomatics, Wuhan University, Wuhan* 430079, *China. E-mail: cjxu@sgg.whu.edu.cn*
[2]*GFZ German Research Centre for Geosciences, Physics of Earthquakes and Volcanoes, Potsdam* 14467, *Germany*
[3]*Key Laboratory of Geospace Environment and Geodesy, Ministry of Education, Wuhan University, Wuhan* 430079, *China*
[4]*Hubei Luojia Laboratory, Wuhan* 430079, *China*
[5]*Institute of Geosciences, University of Potsdam, Potsdam* 14469, *Germany*

SUMMARY

Previous studies have shown that it is difficult to determine whether the 2015 Pishan earthquake occurred on a uniform fault or a ramp-flat fault with variable dip angles due to the similar goodness of data fit to coseismic and afterslip models on these two fault models. Here, we first present the InSAR deformation obtained from both ascending and descending orbits, covering the coseismic period and cumulative 5-yr period after the 2015 Pishan earthquake. We then determine the preferred fault geometry by the spatial distributions between the positive Coulomb failure stress change triggered by main shock and the afterslip. Based on the preferred fault model, we finally use a combined model to determine the contributions of elastic and viscoelastic deformation in the post-seismic deformation. We find that the Pishan earthquake prefers to occur on a ramp-flat fault, and the coseismic slip is mainly distributed at a depth of 9–13 km, with a maximum slip of about 1.3 m. The post-seismic deformation is primarily governed by afterslip, as the poroelastic rebound-induced deformation fails to account for the observed post-seismic deformation and the contributions from the viscoelastic relaxation mechanism can be considered negligible in the combined model. Moreover, the modelled stress-driven afterslip and observed kinematic afterslip have good consistency, and the difference between the root mean square error of the two afterslip models is only 4.3 mm. The results from the afterslip model indicate that both of the updip and downdip directions distribute the afterslip, and slip in the updip direction is greater than that of the downdip direction. Meanwhile, the maximum cumulative afterslip after 5 yr is approximately 0.26 m which is equivalent to a released seismic moment of a M_w 6.47.

Key words: Satellite geodesy; Seismic cycle; Inverse theory; Time-series analysis; Earthquake hazards; Crustal structure.

1 INTRODUCTION

On 3 July 2015, an M_w 6.5 earthquake occurred between Pishan and Yecheng counties in Xinjiang, with the epicentre only 7 km from Pishan County (here referred to as the Pishan earthquake). No trace of a Holocene active fault zone was found within 50 km of the epicentre, indicating that this earthquake occurred on a blind fault (Li *et al.* 2016; Lu *et al.* 2016; Sun *et al.* 2016; Ainscoe *et al.* 2017; Guilbaud *et al.* 2017; Bagnardi & Hooper 2018; Wang *et al.* 2018b, 2020). The earthquake led to three deaths, 214 injuries and severe building collapses (Wang *et al.* 2018b). The collision of the Indian Plate with the Eurasian Plate resulted in the West Kunlun

Mountains and the Tarim Basin squeezing each other, with a relative convergence rate of 5 mm a^{-1} (Xu *et al.* 2011; Li *et al.* 2012; Wang *et al.* 2018b). The earthquake epicentre is situated within the west Kunlun fault zone, positioned at the southwestern periphery of the Tarim Basin, China's most extensive inland basin and the northwestern boundary of the Tibetan Plateau (Fig. 1). This region has long been an important tectonic research area (Matte *et al.* 1996; Kao *et al.* 2001; Li. 2002; Cheng *et al.* 2016). The Tarim Desert Basin is characterized by thick Cenozoic sediments, with thicknesses reaching 10 km (Sobel & Dumitru 1997; Yin *et al.* 2002; Lin *et al.* 2012; Wang *et al.* 2013; Jiang & Li 2014; Lu *et al.* 2016; Ainscoe *et al.* 2017). Lu *et al.* (2016) utilized three high-resolution
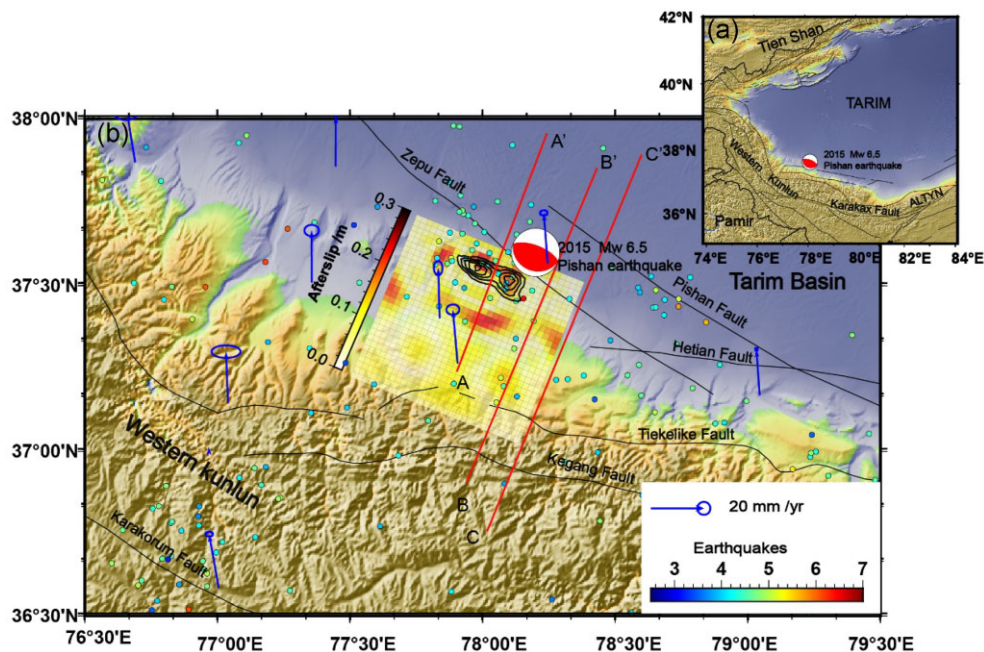
Figure 1. The tectonic background of the 2015 M_w 6.5 Pishan earthquake. Black lines indicate main faults; white–yellow–red patches indicate afterslip distribution; the black contours are coseismic slip distribution; the blue line with an arrow represent velocity field for India–Eurasia measured during 1991–2015(Zheng *et al.* 2017); the colour circles indicate the historical earthquake catalogue (M_w > 2.5 from 01/01/1900 to 04/12/2023); AA', BB' and CC' are part of seismic reflection profiles from Lu *et al.* (2016).

seismic reflection profiles and well drilling data to interpret the Pishan earthquake. They used these data sources to acquire detailed information about the sedimentary cover and lithology in the southwestern Tarim Basin through well drilling, as well as the major layers and faults by analysing the three high-resolution seismic reflection profiles. As a result, they claimed that the Pishan earthquake occurred between two detachment layers at depths of 9–13 km beneath the West Kunlun Mountains and the Tarim Basin. Thrust systems developed above the shallow detachment layer, with a lot of parallel oblique thrust faults distributed between the two detachments (Lu *et al.* 2016). Historically, two medium-strong earthquakes exceeding M_w 6 occurred within 100 km of this earthquake epicentre, an M_w 6.8 earthquake in Pishan, Xinjiang on 31 August 1902 and the other M_w 6.2 earthquake in Pishan, Xinjiang on 29 May 1998. Because of the large recurrence time and the limited observation technology, there is a lack of information for these two earthquakes. Therefore, the 2015 Pishan earthquake provides a valuable opportunity for researching the crustal deformation characteristics beneath the West Kunlun Frontal Thrust Belt.

Tiltmeters, strain gauges and levelling instruments to Global Navigation Satellite Systems (GNSS), Interferometric Synthetic Aperture Radar (InSAR) and optical satellites, geodetic observation techniques have been widely used in seismic fault slip distribution inversion and post-seismic deformation studies (Massonnet *et al.* 1993; Freymuller *et al.* 1993; Peltzer 1999; Fialko *et al.* 2001, 2002, 2005; Fialko 2004; Allison *et al.* 2002; Sandwell *et al.* 2008; Li *et al.* 2009; Lin *et al.* 2009; Liu *et al.* 2009; Shen *et al.* 2009; Zhang *et al.* 2011; Chen *et al.* 2014; Wang *et al.* 2019; Fathian *et al.* 2021; Guo *et al.* 2022; He *et al.* 2022; Li *et al.* 2022). For the 2015 Pishan M_w 6.5 earthquake, only two GNSS campaign stations exist within 50 km of the epicentre (He *et al.* 2016), which makes it challenging to acquire conventional continuous deformation data. However, the co- and post-seismic deformation of this earthquake have been completely captured by Sentinel-1A satellite (Ainscoe *et al.* 2017;

Wang *et al.* 2018b). Therefore, we utilize the Interferometric Synthetic Aperture Radar (InSAR) observations to model the co- and post-seismic deformations of the Pishan earthquake. The coseismic source parameters are compared to independent estimates from broadband seismology.

After the Pishan earthquake, many scholars investigated the seismic source mechanism (He *et al.* 2016; Sun *et al.* 2016; Ainscoe *et al.* 2017; Bagnardi & Hooper 2018; Wang *et al.* 2018b, 2020), geological structure and seismic genesis of this earthquake (Li *et al.* 2016; Lu *et al.* 2016; Guilbaud *et al.* 2017). However, due to differences in data and models used, there were certain discrepancies in the details of the slip distribution and fault geometry, which remains a subject of debate (He *et al.* 2016; Li *et al.* 2016; Lu *et al.* 2016; Sun *et al.* 2016; Ainscoe *et al.* 2017; Bagnardi & Hooper 2018; Guilbaud *et al.* 2017; Wang *et al.* 2018b, 2020). For example, both the geometric model of a non-uniform fault (from seismic reflection profile) and uniform fault can fit the co- and post-seismic deformations well, and we cannot judge the better one (Ainscoe *et al.* 2017). However, such discrepancy result in significant differences in the depth range of fault slip distribution and slip magnitude (Sun *et al.* 2016; Ainscoe *et al.* 2017; Guilbaud *et al.* 2017; Bagnardi & Hooper 2018; Wang *et al.* 2018b, 2020). In this paper, we determine the ramp-flat fault geometry through a combined analysis of slip and stress derived from co- and post-seismic geodetic data. This analysis has the potential to serve as a reference for determining the complex fault geometry in other earthquakes.

2 InSAR OBSERVATIONS

2.1 Coseismic deformation

The July 2015 M_w 6.5 Pishan earthquake was fully covered by Sentinel-1A SAR images launched by the European Space Agency (ESA). The InSAR ascending (T056A) and descending (T136D)

data before and after the event (Table S1) are used to study the co- and post-seismic deformations. We use Interferometric Synthetic Aperture Radar Scientific Computing Environment (ISCE) developed by NASA Jet Propulsion Laboratory (Rosen *et al.* 2018) to process InSAR coseismic deformation data with a multilook ratio of 10:2 between the satellite's range and azimuth directions. The effect of terrain from interferograms are removed by Shuttle Radar Topography Mission (SRTM) Digital Elevation Model (DEM) with a resolution of 90 m, which jointly developed by the NASA, the National Geospatial-Intelligence Agency, and the German and Italian Space Agencies (Farr *et al.* 2007). We use a power spectrum filter to reduce the influence of phase noise and use a branch cut method to unwrap the interferogram (Goldstein & Werner 1998). The interferograms are geocoded using WGS84 geographic coordinates with a resolution of 90 m.

Both of coseismic deformation on ascending and descending tracks show similar double-lobed shapes, which indicate that the Pishan earthquake was primarily characterized by vertical deformation (Figs 2a and c). The coseismic deformation gradient is significant, without obvious noise (Figs 2a and c). The line of sight (LOS) deformation shows uplift in the northwest and subsidence in the southeast, with a maximum uplift of ∼11 cm and a maximum subsidence of ∼4 cm in LOS direction. The observation of greater uplift amplitude than subsidence amplitude points towards the earthquake being predominantly a thrust event. The SAR imagery's superior spatial resolution offers potent spatial constraints for seismic deformation modelling. Nonetheless, utilizing full-resolution InSAR data for modelling demands substantial computing resources, thereby significantly compromising computational efficiency. Consequently, we use a quadtree sampling strategy (Jónsson *et al.* 2002) to sample the full-resolution InSAR data, whereby we densely sample regions with discernible deformation gradients and sparsely sample areas with minor deformation gradients. Following the sampling process, we left with a total of 511 ascending data and 511 descending data (Figs 2b and d).

2.2 Post-seismic deformation

We collect 5 yr of post-seismic deformation on ascending and descending orbits and post-seismic deformation interferograms using the same processing method as for the coseismic deformation analysis. A Digital Elevation Model (DEM) with a resolution of 90 m is used to remove topographic phase from the differential interferogram. Time-series analysis is conducted using the MintPy package (Miami InSAR Time-Series software in Python; Zhang *et al.* 2019), and the ERA5 meteorological data model provided by ECMWF is utilized to remove atmospheric effects (Hersbach *et al.* 2020). The spatiotemporal baseline maps of the Sentinel-1A data are shown in Fig. S1.

Post-seismic deformation patterns in the ascending and descending tracks are similar to coseismic deformation (Figs S2 and S3). To accurately delineate the main area of post-seismic deformation, we locate characteristic points (A–D) on the post-seismic map based on the deformation positions observed on the coseismic map. On the ascending orbit, we set characteristic points A and B at the positive and negative deformation positions, respectively. Additionally, we observe significant signals in the northwest of point A, so we set a characteristic point C at this location (Figs 3a and c). Regarding the post-seismic deformation observed on the descending orbit, we selected only one characteristic point (D) on the descending orbit map. The temporal characteristics of the four characteristic points

all exhibit significant post-seismic deformation features (Figs S2, S3 and S4). For sampling post-seismic deformation, we also use the quadtree sampling strategy (Jónsson *et al.* 2002) to sample the full-resolution InSAR data. As a result, we obtained 514 ascending data and 587 descending data (Figs 3b and d).

3 MODELLING OF COSEISMIC DEFORMATION

3.1 Coseismic fault geometry and slip distribution

The process of inverting coseismic fault slip distribution is commonly divided into two distinct steps (Wright *et al.* 2003; Atzori *et al.* 2009; Feng *et al.* 2013). During the first step, the fault is treated as a uniform plane and its geometric parameters are estimated using non-linear search methods based on the Okada model (Okada 1985). In recent years, commonly methods used for determining fault geometry parameters include Levenberg–Marquardt algorithm (Linde & Johnston 1989), simulated annealing method (Sudhaus & Jo´nsson 2009), and multipeak particle swarm algorithms method (Feng *et al.* 2010), among others. Here, the geometric parameters of the Pishan earthquake fault are determined using the multipeak particle swarm algorithm (Feng & Li 2010). The inversion results show that the strike of the fault is 112.4° and the dip angle is 23.8°, which are consistent with previous studies (He *et al.* 2016; Sun *et al.* 2016; Bagnardi *et al.* 2018). However, seismic reflection profiles indicate a flat (∼3° dip) trajectory of the fault trace below ∼13 km (Ainscoe *et al.* 2017), and a flat detachment layer at about 9 km depth. In between both detachments, the dip angle of the rupture is assumed ∼23.8°. As a result, we have designated the uniform fault as 'Fault Model-1 (FM-1, strike = 121.4°, dip = 23.8°)' and have created a secondary Fault model, named 'Fault Model-2 (FM-2; ramp—flat fault model)', which is based on FM-1. FM-2 is characterized by a shallow dip angle of 3° below a depth of approximately 13 km, while all other parameters remain consistent with those of FM-1.

Upon determining the geometric parameters of the fault, FM-1 and 2 were extended to a length and width of 60 × 60 km², respectively, and divided uniformly into 900 patches of 2 × 2 km². The coseismic slip distribution of each patch was inverted using the non-negative linear least squares algorithm and the Tikhonov regularization algorithm (Ainscoe *et al.* 2017; Tikhonov 1963a, b), with the regularization parameter determined using the variance component estimation method (Schwintzer 1990; Koch & Kusche 2002; Xu *et al.* 2009; Wang *et al.* 2018a; Zhao *et al.* 2022). The coseismic slip distributions of FM-1 and 2 are shown in Figs 4(a) and (d).

3.2 Coulomb failure stress induced by main shock

In this section, we estimate the positive Coulomb failure stress changes (PCFSC) induced by the main shock (Figs 4a and d) on the FM-1 and 2. The Coulomb failure function (ΔCFS) is shown as

$$\Delta CFS = \Delta \tau + \mu' \Delta \sigma \qquad (1)$$

Where $\Delta \tau$ is the shear stress changed, $\Delta \sigma$ is the normal stress changed and μ' is the apparent coefficient friction (Reasenberg & Simpson 1992; Harris 1998). The physical notation of stress is used in eq. (1) (compressive stress negative). The positive Coulomb failure stress changed on fault means promoting failure and negative values means retarding it. In this paper, the Coulomb failure stress
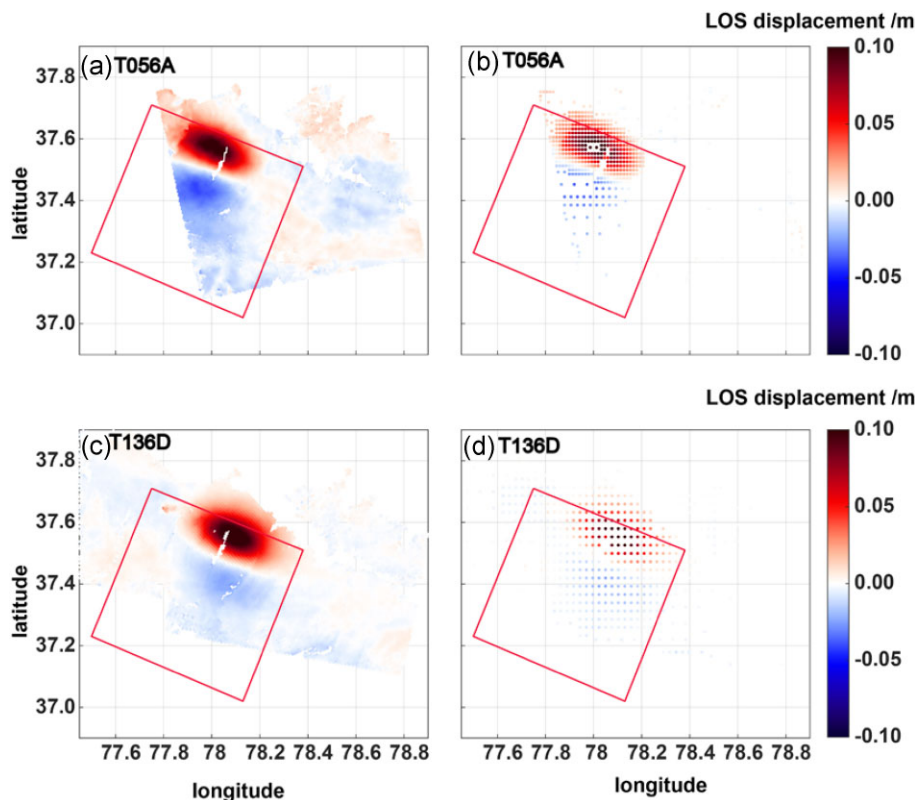
Figure 2. Coseismic deformations for the 2015 Pishan M_w 6.5 earthquake. (a), (c) are full-resolution observations in ascending and descending orbits. (b), (d) are downsampled observations in ascending and descending orbits. The red box represents the surface projection of the fault trace.

changed calculated by the PSGRN-PSCMP program (Wang *et al.* 2006), and the apparent coefficient friction (μ') is set as 0.5. The distributions of PCFSC on FM-1 and 2 are shown in Figs 4(b) and (e). We found the PCFSC are distributed in both of the updip and downdip directions on the FM-1 and 2 (Figs 4b and e).

4 POST-SEISMIC DEFORMATION MECHANISMS SIMULATION

The study of post-seismic deformation mechanisms is a fundamental approach to explore the rheological structure of the lithosphere (Pollitz 2019), which not only fills the temporal gap between seismic elastic waves and postglacial rebound but also characterizes the deep medium properties in active fault zones (Bürgmann & Dresen 2008). The classical post-seismic deformation refers to the delayed changes in the lithosphere caused by stress relaxation in the low-viscosity layer of the mantle or crust (Sabadini & Vermeersen 2004). Currently, the widely accepted post-seismic deformation mechanisms include the poroelastic rebound model in the crust (Peltzer *et al.* 1996; Jónsson *et al.* 2003), aseismic slip on the fault outside the ruptured region (Bürgmann 2018) and viscoelastic relaxation in the lower crust and upper mantle (Burgmann & Dresen 2008; Pollitz 2019). The effects of afterslip and poroelastic response usually occur in the early period, while the viscoelastic relaxation effect lasts for a longer time after the earthquake.

4.1 Kinematic afterslip

Post-seismic afterslip pertains to the fault slip induced by a coseismic perturbation of the stress, which transpires up or down the dip

of the fault (Bürgmann 2018). We calculated the kinematic afterslip by using the cumulative deformation observed via InSAR over a period of 5 yr after the main shock (Figs 4c and f). The inversion approach is identical to that used for the coseismic slip. In general, the spatial distribution of PCFSC induced by the coseismic fault slip are close to the spatial distribution of kinematic afterslip (Diao *et al.* 2021; Zhao *et al.* 2023). Here, the preferred fault model is selected by assessing the consistency between the spatial distribution of PCFSC induced by the coseismic slip on FM-1 and 2 and the spatial distribution of kinematic afterslip on their corresponding faults. On the FM-1, the coseismic slip is distributed between 9 and 13 km (Fig. 4a), while the PCFSC is distributed above and to both sides of the coseismic slip (Fig. 4b). The PCFSC are primarily distributed in the updip and downdip directions, spanning a range of 6–9 km in the updip direction and a range of 11–14 km in the downdip direction (Fig. 4b). Correspondingly, cumulative afterslip over the 5 yr following the main shock was observed to occur in both the updip and downdip directions (Fig. 4c). Specifically, updip afterslip was dispersed within a range of 8–11 km, while downdip afterslip was distributed between 14 and 19 km. Additionally, some minor afterslip events were detected at shallower depths (1–5 km; Fig. 4c). It is evident that a significant discrepancy exists between the spatial distribution of kinematic afterslip and the PCFSC for the model FM-1 (Figs 4b and c).

On the FM-2, the coseismic slip is also distributed between 9 and 13 km (Fig. 4d), and the maximum slip and moment magnitude are similar to those of the FM-1. The PCFSC induced by the main shock is distributed around the coseismic slip (Fig. 4e), with the updip distribution mainly between 7 and 9 km and some weaker positive values distributed between 6 and 7 km in the shallow depths. The downdip PCFSC are mainly distributed between
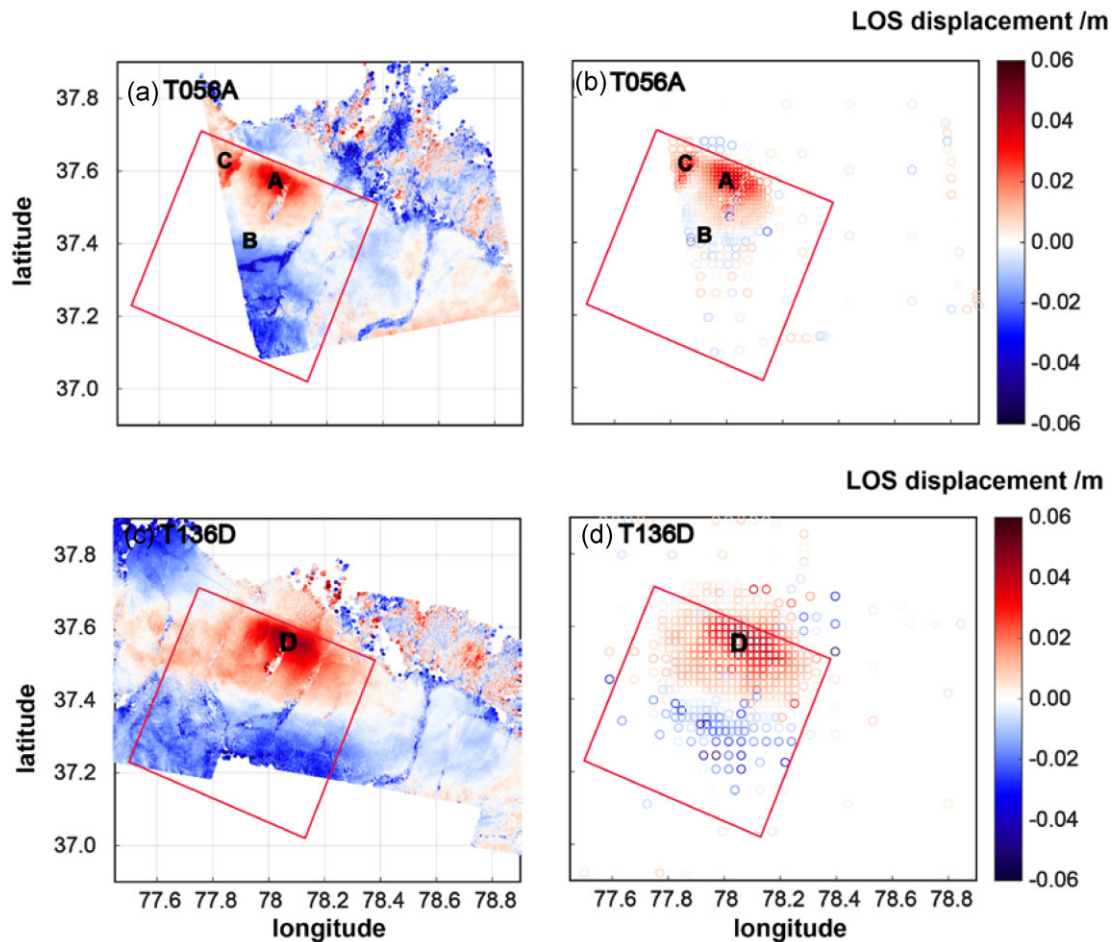
Figure 3. The full resolution and downsampled accumulated LOS displacement ∼5-yr after the main shock. (a), (c) are full-resolution observations in ascending and descending orbits. (b), (d) are downsampled observations in ascending and descending orbits. A–D are characteristic points defined to delineate the post-seismic deformation over 5-yr time. The red box represents the surface projection of the fault trace.

12.8 and 13.3 km, and there are some scattered weak positive values distributed between 13.3 and 14 km (Fig. 4e). Remarkably, the kinematic afterslip over 5 yr after the earthquake is mainly distributed between 8 and 10 km in the updip direction, and there is also a weak afterslip distributed between 6 and 8 km (Fig. 4f). In the downdip direction, it is mainly distributed between 13 and 13.3 km, and there is also a weak afterslip distributed between 13.3 and 14 km (Fig. 4f). It is clear that there exists a robust spatial coherence between the distribution of 'observed' kinematic afterslip and the modelling of PCFSC on the FM-2. From the perspective of consistency between kinematic afterslip and PCFSC, we believe that the fault with a change in dip at around 13 km is more in line with the seismogenic fault of this earthquake, which supports the results of the seismic reflection profile (Lu *et al.* 2016).

4.2 Poroelastic rebound

Poroelastic rebound is assumed to occurring at shallow depths in the Earth's crust, especially in water-saturated sediments with high porosity. The poroelastic response reflects the transformation of pore water pressure from a non-equilibrium state to an equilibrium state caused by coseismic slip. The flow of pore water causes surface displacement, which usually takes only a few months (Nur 1972; Peltzer *et al.* 1996; Jónsson *et al.* 2003). The drained and undrained Poisson's ratios are commonly used to represent the instantaneous

deformation immediately after the earthquake and the deformation short time after the earthquake when the pore water pressure had time to develop a new equilibrium state. Therefore, it is possible to calculate the poroelastic rebound deformation by inverting for coseismic slip twice, once with the undrained Poisson's ratio and once with the drained Poisson's ratio, and then using the difference in surface displacement to estimate the poroelastic contribution to surface movement after the earthquake (Huang et al 2014; Diao *et al.* 2021, Table S2)**.** We found that the poroelastic surface deformation is more southward compared to the observed movement after the earthquake (Figs 3 and 5). Because the predicted pattern is very different to observations, we conclude that the poroelastic effect was not dominant in the post-seismic deformation for the Pishan earthquake.

4.3 Viscoelastic relaxation

The viscoelastic relaxation mechanism considers the post-seismic deformation caused by a coseismic stress disturbance that is transmitted deep into the lower crust and upper mantle. This deformation occurs at the Earth's surface over a long timescale and a broad spatial area (Burgmann & Dresen 2008; Pollitz 2019). Because of the post-seismic deformation used in this study over a long period, it is necessary to consider the viscoelastic relaxation mechanism. To investigate whether the viscoelastic relaxation effect could have
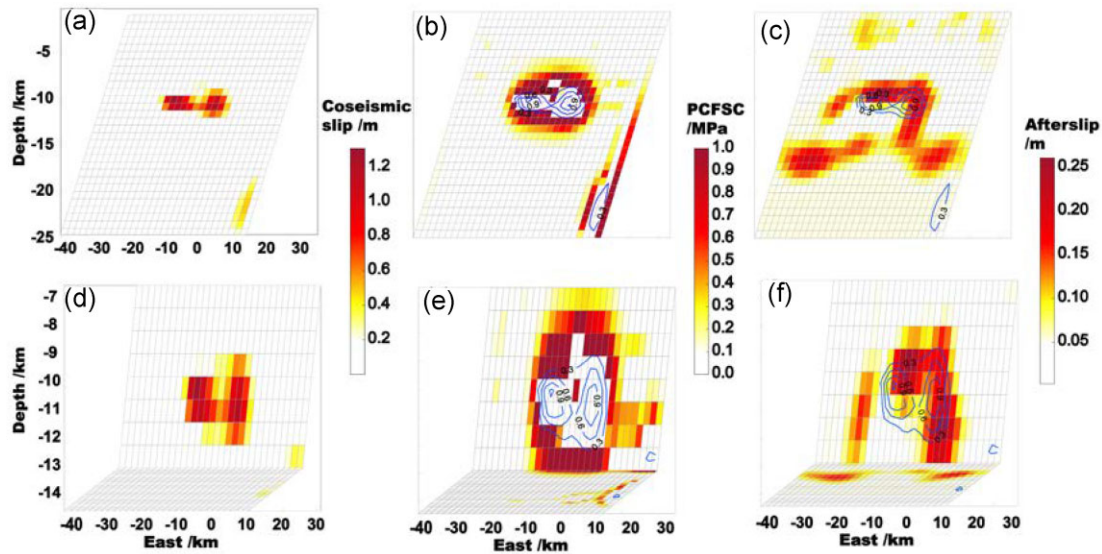
Figure 4. The distributions of coseismic slip, positive Coulomb failure stress changes (PCFSC) induced by the main shock and afterslip of the FM-1 and 2. (a), (d) are the coseismic slip distributions of the FM-1 and 2; (b), (e) are distributions of positive coseismic Coulomb failure stress change of the FM-1 and 2; (c), (f) are the kinematics afterslip distributions after 5 yr of the FM-1 and 2: The blue contours in (b), (e), (c), (f) represent the location of the coseismic slip distribution, and the black numbers indicate the slip magnitude.
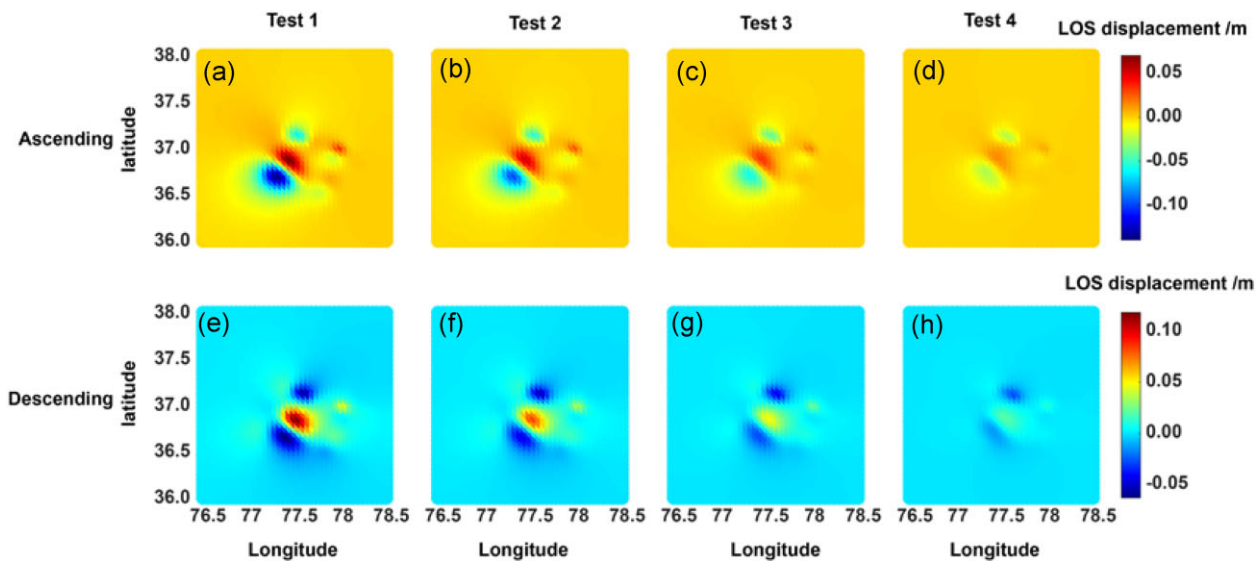

Figure 5. The full resolution deformation predicted by the Poroelastic rebound model. The first row represents the ascending orbit deformation and the second row represents the descending orbit deformation. (a, e) Poisson's ratios under the undrained (0.25) and drained conditions (0.05); (b, f) Poisson's ratios under the undrained (0.25) and drained conditions (0.1); (c, g) Poisson's ratios under the undrained (0.25) and drained conditions (0.15); (d, h) Poisson's ratios under the undrained (0.25) and drained conditions (0.2).

played a role in the post-seismic deformation of the Pishan earthquake over the 5-yr period, we first define the local internal structure of our Earth using CRUST 1 (Laske *et al.* 2013, Table S3). We set the depth of the Moho discontinuity at 43.26 km and used the PS-GRN_PSCMP software package to calculate the surface deformation pattern caused by viscoelastic relaxation due to stress released by coseismic slip distribution (Wang *et al.* 2006). We found that the surface deformation caused by viscoelastic relaxation exhibits good spatial consistency with the observed deformation (Fig. 6). For example, in the descending orbit (T136D), viscoelastic relaxation deformation has a larger range than observed deformation, and the deformation pattern and location is similar to the observed deformation (Figs 6c and d). In the ascending orbit (T056A), the location of

negative deformations is close to the observed observations (Figs 6a and b). Therefore, we cannot subjectively rule out the contribution of viscoelastic relaxation to the post-seismic deformation in the Pishan earthquake.

4.4 Post-seismic deformation explained by the combined model

The post-seismic deformation mechanisms of poroelastic rebound, afterslip and viscoelastic relaxation may act simultaneously in most cases (Freed *et al.* 2006; Gunawan *et al.* 2014; Huang *et al.* 2016). Therefore, geodetic measurements may contain a comprehensive
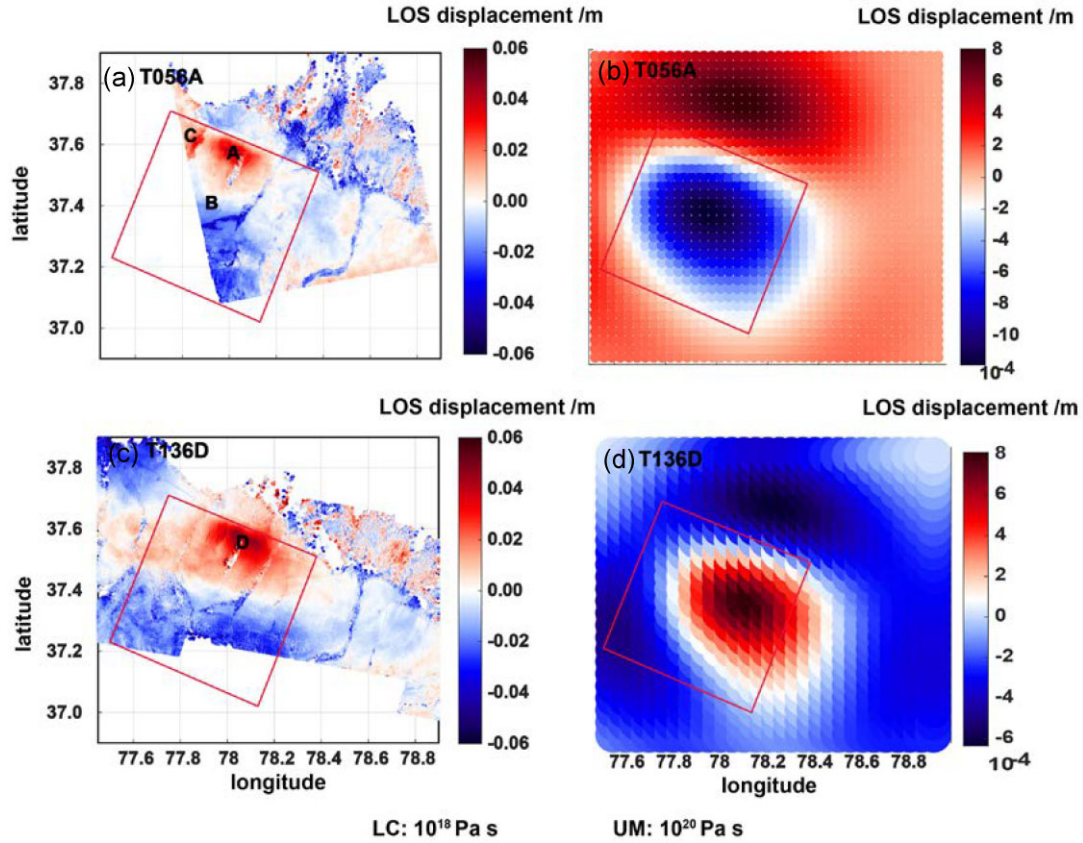
Figure 6. The deformation predicted by the viscoelastic relaxation model. LC: lower crust, UM: upper mantle. (a) and (c) are the observed data in the ascending and descending tracks; (b) and (d) are the deformation predicted by the viscoelastic relaxation model in the ascending and descending tracks.

effect of these three mechanisms. Although existing research suggests that it is very difficult to strictly distinguish the interactions of three mechanisms, there is still hope to clarify the contributions of different mechanisms with the effective capture of relaxation deformation signals in the temporal and spatial domains of spatial earth measurements (Fialko 2004; Rousset *et al.* 2012; Diao *et al.* 2021; Jin *et al.* 2022, 2023; Zhao *et al.* 2023). For example, Fialko (2004) jointed poroelastic rebound and kinematical afterslip model to simulated post-seismic deformation of the 1992 M_w 7.3 Landers earthquake, and suggested that the combined simulation can explain the surface relaxation deformation well. Rousset *et al.* (2012) developed a model that integrates afterslip and viscoelastic flow to explain deformation induced by coseismic stress changes of the 1999 M_w 7.6 Chi-Chi earthquake. This model aligns with the shorter relaxation times observed in the immediate vicinity, attributed to ongoing fault movement, as well as the longer characteristic relaxation times and the reverse direction of vertical displacements observed to the east of the Central Range. Diao *et al.* (2021) conducted a comprehensive simulation of the contributions of viscoelastic relaxation and stress-driven afterslip model to the 4-yr cumulative deformation after the main shock using GPS observations and finite element model. Jin *et al.* (2023) constructed a fully coupled model that integrates stress-driven creep within a deep, localized shear zone and viscoelastic relaxation throughout the lower crust to explain the post-seismic deformation of the 2021 M_w 7.3 Maduo earthquake. The data in the mid- to near-field can be adequately explained by taking into account deep afterslip and/or non-Maxwellian viscoelastic behaviour.

Effects of stress-driven afterslip and viscoelastic relaxation are both controlled by the positive Coulomb stress released during the main shock, and typically both processes occur simultaneously after an earthquake. Diao *et al.* (2021) proposed a linear relationship and represent the stress-driven afterslip by multiplying the PCFSC by a constant (*a*). Drawing upon this concept, the post-seismic deformation can be expressed as follows (Diao *et al.* 2021).

$$D(r, t) = D_{cv}(r, t) + a \sum_{rc} \frac{C_p(r_c)}{\tau}$$

$$\left[D_{ae}(r, r_c)\tau \left(1 - e^{(-t/\tau)}\right) + \int_0^t D_{av}(r, t - t', r_c) e^{-t'/\tau} dt' \right]. \quad (2)$$

Namely, the interrelated post-seismic deformation is composed of three parts. The first part D_{cv} is the viscoelastic relaxation deformation caused by coseismic slip. The second part is caused by stress-driven afterslip ($a \sum_{rc} \frac{C_p(r_c)}{\tau} \times D_{ae}(r, r_c)\tau(1 - e^{(-t/\tau)})$). The third part is the viscoelastic relaxation deformation caused by the afterslip ($a \sum_{rc} \frac{C_p(r_c)}{\tau} \times \int_0^t D_{av}(r, t - t', r_c)e^{-t'/\tau} dt'$). Where r means the position of observations; r_c means the position of fault patches; t is the cumulative time after main shock; $C_p(r_c) = max[\Delta CFS(r_c), 0]$ means the PCFSC; ΔCFS means the distribution of Coulomb failure stress change on the fault patches; τ means the decay time of afterslip; D_{ae}, D_{av} are the Green functions correspond to elastic and viscoelastic deformation.

Based on the above theory, we use the FM-2 to calculate the interrelated contributions of viscoelastic relaxation and stress-driven
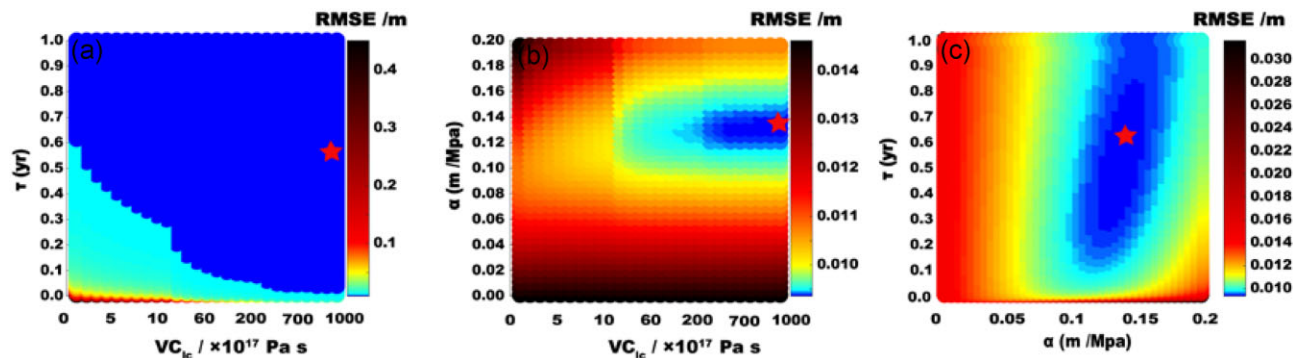
Figure 7. Root mean square errors (RMSE) plotted as function of model parameters (τ, VC_{lc}, α) in the joint inversion. The optimal parameters were determined by the full grid search over model space. The red star represents the optimal position of parameters.

afterslip in the post-seismic cumulative deformation. The post-seismic deformation of 5 yr was divided into 26-time intervals (24, 48, 120, 144, 168, 216, 240, 264, 312, 456, 504, 528, 564, 612, 636, 660, 828, 984, 1068, 1164, 1200, 1284, 1368, 1548, 1656 and 1824 d). The earlier time intervals were divided more tightly, while the later spanned a longer period. The cumulative deformation of each time interval was calculated, and an observation function was constructed based on eq. (2). The contribution of stress-driven afterslip and viscoelastic relaxation mechanisms in the post-seismic deformation of the Pishan earthquake was calculated by the procedures introduced in Diao *et al.* (2021). We estimate an interrelation constant of $\alpha = 0.136$ m MPa^{-1}, $i = 27$ ($VC_{lc} = 10^{20}$ Pa s) and $\tau = 0.53$ yr (Fig. 7). Diao *et al.* (2021) used the same method to investigate the overlapping effects of afterslip and viscoelastic relaxation after the 2015 Gorkha earthquake and obtained similar values for α (0.18 m MPa^{-1}) and τ (0.6 yr) close to we did. Additionally, our findings indicate that earthquakes of different magnitudes may exhibit similar relaxation times for post-seismic afterslip. The optimal lower crustal viscosity coefficient reached its up bound (Fig. 7), indicating that the Pishan earthquake occurred in the pure brittle upper crust.

5 DISCUSSION

5.1 Fault slip distribution

After the earthquake, several groups analysed Pishan earthquake based on different data, and the majority of scholars believe that this earthquake occurred on a uniform fault plane (He *et al.* 2016; Sun *et al.* 2016; Bagnardi & Hooper 2018). Only a few studies included structural and fault information from seismic reflection profiles (Ainscoe *et al.* 2017; Wang *et al.* 2018b). However, approaching the problem from the perspective of fitting the coseismic and post-seismic data alone cannot determine whether the earthquake occurred on a uniform fault plane or a geological fault, as both models can fit the observed surface deformation well (Ainscoe *et al.* 2017). Drawing on geodetic data, this paper examines the spatial consistency between the distribution of the PCFSC triggered by main shock and the distribution of kinematic afterslip. It is found that assuming a ramp-flat thrust fault (model FM-2), the distribution of PCFSC is spatially consistent with the kinematic afterslip. In addition, the stress-driven afterslip introduced in this paper is obtained by multiplying the PCFSC triggered by the main shock with a proportionality coefficient α of 0.136 m MPa^{-1}. Meanwhile, we observed that the root-mean-square errors (RMSE) between the surface deformation predicted by both stress-driven and

kinematic afterslip and the observed deformation were 11.5 and 7.2 mm, respectively. The weak difference of RMSEs indicates that both stress-driven afterslip and kinematic afterslip can reproduce the observations well. This finding reinforces the idea that stress-driven and kinematic afterslip can mutually support each other on a ramp-flat fault, thereby increasing the dependability of FM-2.

Different fault geometries and data can lead to slightly different results in the distribution of coseismic fault slip (Li *et al.* 2016; Lu *et al.* 2016; Sun *et al.* 2016; Ainscoe *et al.* 2017; Guilbaud *et al.* 2017; Bagnardi & Hooper 2018; Wang *et al.* 2018b, 2020). Regarding the coseismic slip distribution of the Pishan earthquake, previous studies have shown that this earthquake was dominated by thrust slip, and most studies indicate that the fault slip did not rupture to the surface, with rupture depths mainly concentrated at 8–16 km and the maximum slip of 0.6–1.2 m. The moment magnitudes were estimated to be between M_w 6.3 and 6.5 (Ainscoe *et al.* 2017; Bagnardi & Hooper 2018; Wang *et al.* 2018b).

Based on our fault models FM-1 and 2, we use a non-negative constrained least squares method to invert the coseismic slip distribution. Both models show that the coseismic slip is concentrated within a range of 20 × 11 km, with a maximum slip of approximately 1.3 m, and a released seismic moment of 5.435×10^{18} N m (5.776×10^{18} N m), equivalent to an earthquake with a magnitude of M_w 6.46 (M_w 6.47) (Figs 4a and d). These results are similar to those reported by Ainscoe *et al.* (2017). The RMSEs between the coseismic surface deformation predicted by FM-1 and 2 and the observed deformation are 12 and 11.8 mm, respectively. These results account for approximately one-tenth of the maximum coseismic deformation. The striking similarity between the two coseismic slip models can be attributed primarily to the fact that the fault slip is mainly concentrated on the same oblique fault located above 13 km, while no obvious continuous slip occurs below 13 km and above 9 km. Although the data fitting results of using non-negative least squares to invert the coseismic slip distribution in this paper may be slightly worse than those obtained by least squares inversion (Fig. S5), it can better concentrate the slip distribution, which is consistent with the results from Ainscoe *et al.* (2017). By the way, we found that the moment magnitude derived from seismic wave data is smaller than the results from InSAR observations. This may be due to the longer observation period of InSAR data, which includes some post-seismic deformation (USGS; He *et al.* 2016; Wen *et al.* 2016; Ainscoe *et al.* 2017). However, the fault geometry parameters derived from seismic wave and InSAR data are similar (He *et al.* 2016; Ainscoe *et al.* 2017). Furthermore, He *et al.* (2016) utilized differential calculations of GPS coseismic deformation based on
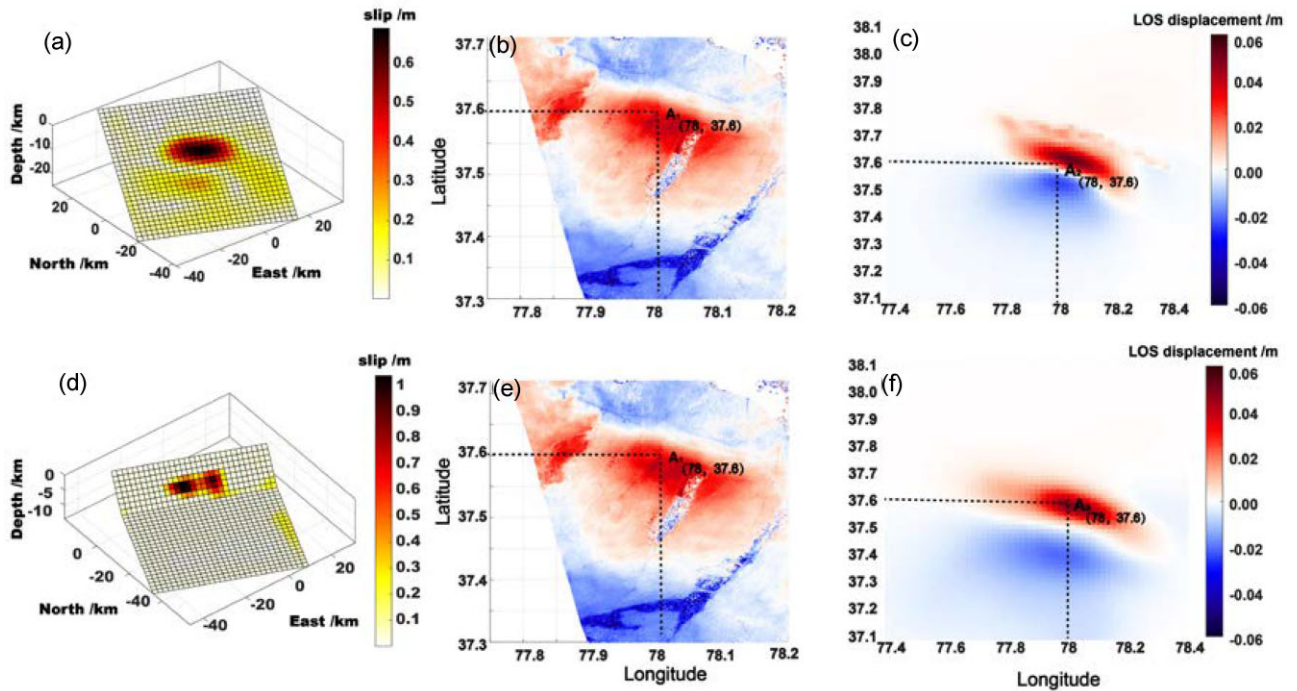
Figure 8. The deformation forward by stress-driven afterslip with the different depths range of coseismic slip distributed. Panels (a) and (d) are coseismic slip distributions with depths range of 7–16 km and 9–13 km; panels (b) and (e) are post-seismic observed deformations; panels (c) and (f) are deformations resulting from stress-driven afterslip.

data recorded by campaign GPS measurements before and after the earthquake. This coseismic deformation encompassed early post-seismic deformation over a 1-month period. Based on this GPS observations, they inverted for a slip distribution concentrated at a depth of 10–12 km, yielding a moment tensor of 6.42×10^{18} N·m, equivalent to an M_w 6.48 earthquake. These findings closely align with results obtained from InSAR data that also incorporated early post-seismic deformation.

Several studies indicated that the depth of coseismic slip distribution reaches shallower than 8 km in the updip direction and deeper than 13 km in the downdip direction (He *et al.* 2016; Sun *et al.* 2016; Wen *et al.* 2016). However, from the perspective of stress-driven afterslip, such depth seems unreasonable in the Pishan event. Due to the fact that the PCFSC triggered by the coseismic slip distribution typically distributes around the ruptured patch, slip distributions at deeper or shallower depths would result in the PCFSC that distributes deeper or shallower as well. As a result, the surface deformation forward by the stress-driven afterslip model may show positional differences from the observed deformation. For example, when the coseismic slip is distributed between 7 and 15 km underground (Fig. 8a), the corresponding surface deformation forward by the stress-driven afterslip is shown in Fig. 8(c). We see that the deformation caused by stress-driven afterslip is farther north compared to the observed deformation (Fig. 8b). For example, points A1 and A2 represent the same coordinates and correspond to the maximum deformation position in the observed deformation field (Fig. 8b), while in the stress-driven afterslip (Fig. 8c), they only represent the boundary between positive and negative deformation (Fig. 8c). The position deviation of A1 and A2 by about 2 km in the north–south direction, with the deformation resulting from stress-driven afterslip being further north than observations. Furthermore, the observations only cover a range of about 4 km in north–south direction, and this difference accounts for half of the deformation

width. When the slip distribution depth is within the range of 9–13 km (Fig. 8d), the surface deformation forward by stress-driven afterslip are consistent in terms of observation pattern and location (Fig. 8f). Therefore, from the perspective of stress-driven afterslip, we consider the coseismic slip distribution depth within 9–13 km to be more reasonable. Typically, afterslip and aftershocks occur within the high PCFSC triggered by the main shock, exhibiting a certain degree of spatial overlap (Huang *et al.* 2017). Precisely relocated aftershock data show that during the week following the earthquake, the majority of aftershocks with high stability were concentrated at depths shallower than 14 km, consistent with the distribution of the FM-2 downdip afterslip (Fig. S6). This further corroborates the reasonability of FM-2. The occurrence of coseismic slip between two detachment layers limits the slip towards further upward or downward directions during the main shock.

5.2 Post-seismic deformation mechanism following the 2015 Pishan earthquake

Due to differences in the surface deformation patterns and position caused by the poroelastic rebound model and observation, the contribution of this mechanism was first excluded. A combined model was used to determine the contributions of stress-driven afterslip and viscoelastic relaxation mechanisms in post-seismic deformation (Diao *et al.* 2021). It has been discovered that even though the long-time span for post-seismic deformation in this study, the deformation resulting from the viscoelastic relaxation mechanism was nearly insignificant (Figs S7 and S8). This was due to the viscosity coefficient in the lower crust of the area reaching the search upper boundary (10^{20} Pa s), which was caused by a thickness at least 44 km of crust in the region (Ainscoe *et al.* 2017). Kinematic afterslip and positive Coulomb stress distribution indicate that afterslip primarily occurs in the upper crust at depths ranging from
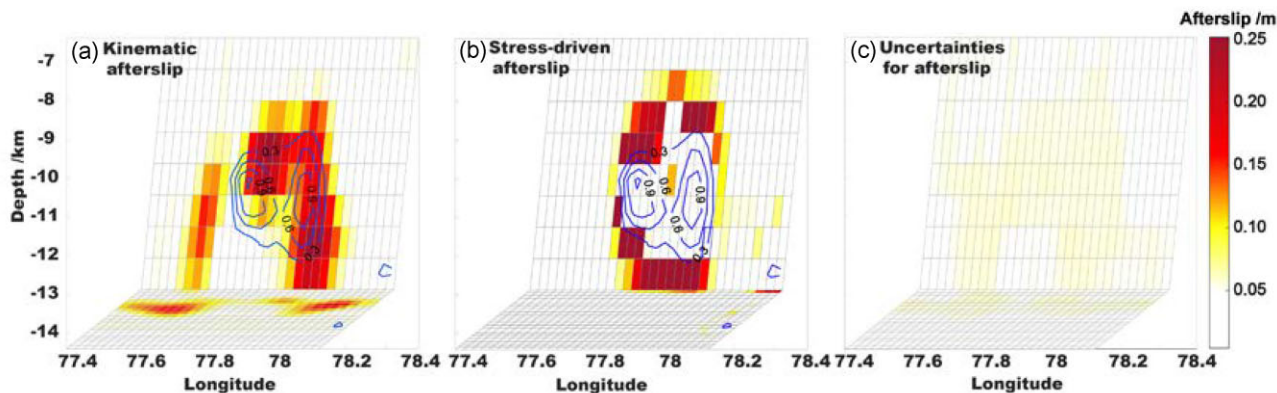
Figure 9. Results of the uncertainty analysis of afterslip. The distributions of afterslip (a, b) and uncertainties (c) for the kinematic afterslip. The blue contours in (a), (b) represent the location of the coseismic slip distribution, and the black numbers indicate the slip magnitude.

8 to 14 km, well above the crust–mantle boundary. The positive Coulomb stress distributed in this depth is insufficient to induce viscoelastic deformation. Furthermore, we tested, under the condition of the absence of viscoelastic relaxation deformation mechanisms, the determination of stress relaxation time and the proportional coefficient between stress-driven relaxation and PCFSC using the method proposed by Diao *et al.* (2021). We found that the results for τ and α were close to the results from combined models ($\alpha = 0.131$ m MPa^{-1} and $\tau = 0.45$ yr; Fig. S9). This indicates that the contribution of the viscoelastic relaxation model to post-seismic deformation in the Pishan earthquake can be neglected, and the post-seismic deformation in the Pishan earthquake for 5 yr after the event was dominated by afterslip. All Coulomb stress generated by the coseismic rupture was released through afterslip, indicating that this earthquake was a pure elastic rupture event that occurred in the upper crust. The results of the combined model indicate that the magnitude of afterslip reaches its maximum around 500 d after the earthquake, and thereafter it will remain basically stable (Figs S7 and S8).

There have been few studies on post-seismic deformation of the earthquake, with only a few scholars studying the afterslip (Ainscoe *et al.* 2017; Wang *et al.* 2020). Wang *et al.* (2020) studied the kinematic afterslip using the cumulative deformation 447 d after the main shock. However, we found that there were some controversies in his results of the afterslip, such as the fact that afterslip usually accumulates rapidly in the initial period after the main shock and then gradually slows down and reaches a stable state over time. However, the results of Wang *et al.* (2017) showed that there was less afterslip accumulation in the first 255 d, and a large magnitude of afterslip accumulation suddenly appeared in the later period, with the depth of afterslip distribution breaking through the surface, which is inconsistent with the fact that the Pishan earthquake is a blind fault earthquake. Ainscoe *et al.* (2017) calculated the cumulative afterslip using InSAR deformation for 7 months after the main shock, and the inversion results showed that the afterslip surrounded the coseismic slip distribution, with a maximum slip of about 0.35 m and an afterslip depth distribution of 8.5–15 km. He *et al.* (2016) conducted two GPS monitoring campaigns, one at 1 month and the other at 4 months after the earthquake. Each campaign lasted for 2–4 d. Based on a uniform model, they roughly calculated the kinematic afterslip. The calculation results indicated that afterslip was mainly distributed between 5 and 18 km with a maximum slip of 0.2 m. This released a geodetic moment of 4.03×10^{18} N·m, corresponding to an event with a magnitude M_w 6.3.

Kinematic afterslip primarily results from the cumulative deformation over 5 yr following an earthquake. It is calculated based on the Okada model (okada 1985), using a least-squares method with regularization constraints. However, under the assumption of the rate-state friction law, stress-driven afterslip is determined by multiplying the PCFSC triggered by the coseismic event with a linear coefficient α. When the effects of pore elastic rebound and viscoelastic relaxation mechanisms on post-seismic deformation can be safely neglected, stress-driven afterslip and kinematic afterslip exhibit overall consistency. Our findings reveal that both stress-driven afterslip and kinematic afterslip manifest themselves in proximity to the coseismic slip distribution, exhibiting a wider and more scattered distribution pattern compared to the coseismic slip (Figs 9a and b). The updip afterslip is greater than the downdip afterslip, with a maximum displacement of 0.26 m, approximately one-fourth of the maximum coseismic slip. The updip kinematic afterslip and the coseismic slip have a certain overlap (8–10 km), while there is no obvious overlap of downdip kinematic afterslip and the coseismic slip (13.3–14 km; Fig. 9a). The afterslip in the downdip direction mainly occurs on a gently dipping flat fault (3°), located on the boundary of the detachment layer, with a smaller magnitude of slip, which may be related to the magnitude of coseismic rupture and the occurrence of this earthquake between two detachment layers. The accumulated kinematic afterslip for 5 yr after the earthquake released a total seismic moment of 5.622×10^{18} N m, equivalent to a M_w 6.47 coseismic main shock. The main difference between the kinematic afterslip results of this study and Ainscoe *et al.* (2017) lies in the depth distribution of the downdip direction, which is shallower in this study (13.3–14 km) and deeper in Ainscoe *et al.* (2017) (12–16 km), mainly due to the different fault structures used in the two studies. In addition, to test the uncertainty of the kinematic afterslip model, 100 sets of normally distributed random noises with mean of 0 and standard deviation of one-tenth of the maximum are added to observed deformation. The afterslip distribution is inverted for 100 times, and the standard deviation distribution of these slip distributions show that the maximum standard deviation is less than 10 per cent of the maximum afterslip, indicating that the afterslip model in this paper is stable (Fig. 9c).

5.3 Tectonic implication

Results from three seismic reflection profiles from the edge of the Western Kunlun Mountains to the Tarim Basin indicate that there

are a large number of anticlinal thrust structures distributed in the northern part of the Tibetan Plateau, and thick sedimentary deposits are distributed in shallow depths (Li *et al.* 2016; Lu *et al.* 2016). Multiple nearly parallel detachment layers are distributed from shallow to deep at the junction of the Tarim Basin and the Western Kunlun Mountains, jointly controlling the deformation of the Western Kunlun Mountains (Pei *et al.* 2011; Si *et al.* 2011; Lu *et al.* 2016). The 2015 M_w 6.5 Pishan earthquake occurred between two typical detachment layers (D1: 9 km, D2: 13 km). Near the edge of the Western Kunlun Mountains, multiple parallel dipping thrust faults connect the two detachment layers (Lu *et al.* 2016). These duplex parallel dipping thrust faults vertically cut through the entire Proterozoic stratum, but did not reach the Cenozoic strata (Lu *et al.* 2016). The Pishan earthquake occurred on one of the thrust faults, which has a dip angle of 24° at a depth of 9–13 km and a gentler dip angle close to horizontal at the boundary of 13 km underground. This geological structure caused the coseismic slip of the Pishan earthquake to occur within the 9–13 km depth range. The afterslip cannot slip extensively to deeper areas, which is consistent with our FM-2. Most previous studies suggest that the Pishan earthquake occurred on a blind fault earthquake, and field observations within 50 km of the epicentre did not reveal any obvious surface rupture. The main reason for the occurrence of blind fault earthquakes is that the distribution of coseismic slip is limited to the width between two detachment layers. The thickly deposited sediment layers at shallow depths is not accumulating sufficient shear stress to promote rupture to propagate to the surface.

Afterslip is usually triggered by Coulomb stress released during the main shock (e.g. Bürgmann 2018). Based on the rate-and-state friction law, earthquake nucleation occurs in the area of velocity weakening, while afterslip occurs in the velocity strengthening area away from the rupture zone (Marone 1998; Avouac 2015). The occurrence of downdip afterslip may be caused by increased pressure and temperature at depth, resulting in the transfer from velocity weakening to velocity strengthening friction. There are some reasons that can explain why the updip afterslip is larger than the downdip afterslip. On one hand, fluids may play a role at shallower depth and facilitate afterslip. On the other hand, there may be differences in fault friction between the detachment layers in the updip and downdip areas. In addition, a large number of aftershocks occurred between the two detachment layers, indicating that the fault activity in the region is strong (Lu *et al.* 2016). The geological structure makes it highly probable for the occurrence of future blind fault earthquakes in the region.

6 CONCLUSIONS

The co- and post-seismic InSAR deformations, Coulomb failure stress and post-seismic deformation modelling are used to reveal that the 2015 Pishan earthquake occurred on a ramp-flat fault at a depth of 9–13 km. From the perspective of geodetic measurements, it supports the fault structure indicated in seismic reflection profiles. The fault is distributed between two detached layers, limiting the range of slip distribution. The results of a joined inversion of interrelated processes show that the contribution of the viscoelastic relaxation mechanism to post-seismic deformation is negligible. Moreover, the consistency between the kinematic and stress-driven afterslip, as well as the distributions of coseismic slip and afterslip are above 14 km, all indicate that this earthquake is a pure brittle rupture that occurred in the upper crust, and post-seismic deformation is dominated by afterslip. In addition, a large number of aftershocks occurred near the fault after the earthquake, suggesting heightened activity along the fault in the region and a potential occurrence of blind thrust earthquakes in the future.

DATA AVAILABILITY

Sentinel-1 SAR images were downloaded from the Sentinel-1 Scientific Data Hub (https://search.asf.alaska.edu/#/). Fig. 1 is plotted using Generic Mapping Tools (GMT).

SUPPORTING INFORMATION

Supplementary data are available at *GJI* online.

Figure S1. Spatio-temporal baseline of the post-seismic interferometric pairs of the Sentinel-1 tracks.
Figure S2. Post-seismic LOS displacement time-series within 5 yr of ascending tracks 56. A–C are characteristic points defined to delineate the post-seismic deformation over 5-yr time.
Figure S3. Post-seismic LOS displacement time-series within 5 yr of descending tracks 136. D is characteristic point defined to delineate the post-seismic deformation over 5-yr time. black arrows mean the changed negative deformation.
Figure S4. Time-series cumulative deformation of points A, B, C and D 5 yr after the Pishan earthquake.
Figure S5. The coseismic and post-seismic observations fitting and those forward by the slip distributions on fault models 1 and 2.
Figure S6. The distribution of relocated aftershocks one week after the main shock ($M_w > 2.0$). Panels (a), (b) the relocated aftershocks distributed along-dip of the two fault geometries, (c) 3-D graph, (d) bar chart of the distribution of relocated aftershocks counts with respect to depth [the relocated results of the aftershocks are from Lu *et al.* (2016)]. The blue and black error bars in (b) indicate the standard deviation (per km) of the precisely relocated aftershocks above and below a depth of 15 km, respectively. StdH refers to the standard deviation in the horizontal direction, while StdV refers to the standard deviation in the vertical direction.
Figure S7. Contribution of mechanisms of cumulative deformation for 5 yr after main shock in ascending orbit. Each line represents a different time period. The first column represents the observed deformation, and the second column represents the forward deformation of the combined model. The third column represents the deformation forward by afterslip and the fourth column represents the viscoelastic relaxation deformation.
Figure S8. Contribution of mechanisms of cumulative deformation for 5 yr after main shock in descending orbit. Each line represents a different time period. The first column represents the observed deformation, and the second column represents the forward deformation of the combined model. The third column represents the deformation forward by afterslip and the fourth column represents the viscoelastic relaxation deformation.

Figure S9. Root mean square errors (RMSE) plotted as function of model parameters (τ, α).

Table S1. Details of SAR data.

Table S2. The setting of Poisson's ratios corresponding to the co- and post-seismic conditions (undrained and drained) in the poroelastic rebound model.

Table S3. Preferred earth model consisting of elastic lower crust, viscoelastic lower crust and upper mantle.

Please note: Oxford University Press is not responsible for the content or functionality of any supporting materials supplied by the authors. Any queries (other than missing material) should be directed to the corresponding author for the paper.

REFERENCES

Ainscoe, E.A., Elliott, J.R., Copley, A., Craig, T.J., Li, T., Parsons, B.E. & Walker, R.T. 2017. Blind thrusting, surface folding, and the development of geological structure in the Mw 6.3 2015 Pishan (China) earthquake, *J. geophys. Res.,* **122**, 9359–9382.

Allison, J., Sandwell, D., Fialko, Y. & Sichoix, L. 2002. The 1999 (Mw 7.1) Hector Mine, California, Earthquake: near-field post-seismic deformation from ERS interferometry, *Bull. seism. Soc. Am.,* **92**(4), 1433–1442.

Atzori, S., Salvi, S., Antonioli, A. & Tolomei, C. 2009. Finite fault inversion of DInSAR coseismic displacement of the 2009 L'Aquila earthquake (central Italy), *Geophys. Res. Lett.,* **36**(15), doi:10.1029/2009GL039293.

Avouac, J.P. 2015. From geodetic imaging of seismic and aseismic fault slip to dynamic modeling of the seismic cycle, *Annu. Rev. Earth planet. Sci.,* **43**(1), 1–39.

Bagnardi, M. & Hooper, A. 2018. Inversion of surface deformation data for rapid estimates of source parameters and uncertainties: a Bayesian approach, *Geochem. Geophys. Geosyst.,* **19**, 2194–2211.

Burgmann, R. & Dresen, G. 2008. Rheology of the lower crust and upper mantle: evidence from rock mechanics, geodesy, and field observations. *Annu. Rev. Earth planet. Sci.,* **36**, 531–567.

Bürgmann, R. 2018. The geophysics, geology and mechanics of slow fault slip, *Earth planet. Sci. Lett.,* **495**, 112–134.

Chen, Q., Cheng, H.Q., Yang, Y.H., Liu, G.X. & Liu, L.Y. 2014. Quantification of mass wasting volume associated with the giant landslide Daguangbao induced by the 2008 Wenchuan earthquake from persistent scatterer InSAR, *Remote Sens. Environ.,* **152**, 125–135.

Cheng, X., Chen, H., Lin, X., Wu, L. & Gong, J. 2016. Geometry and kinematic evolution of the Hotan-Tiklik segment of the western Kunlun thrust belt: constrained by structural analyses and apatite fission track thermochronology, *J. Geol.,* **125**(1), 65–82.

Diao, F., Wang, R., Xiong, X. & Liu, C.(2021). Overlapped post-seismic deformation caused by afterslip and viscoelastic relaxation following the 2015 Mw 7.8 Gorkha (Nepal) earthquake, *J. geophys. Res.,* **126**, e2020JB020378.

Farr, T.G. et al., , 2007. The shuttle radar topography mission, **45**(2), doi: 10.1029/2005RG000183.

Fathian, A., Atzori, S., Nazari, H., Reicherter, K. & Yaminifard, F. 2021. Complex co- and post-seismic faulting of the 2017–2018 seismic sequence in western Iran revealed by InSAR and seismic data, *Remote Sens. Environ.,* **253**, doi:10.1016/j.rse.2020.112224.

Feng, W.P. & Li, Z.H. 2010. A novel hybrid PSO /simplex algorithm for determining earthquake source earthquake parameters using InSAR data, *Prog. Geophys.,* **24**(4), 1189–1196.

Feng, W.P., Liu, G.C., Li, Z.H. & Shi, X.W. 2013. The 2011 Mw 6.8 Burma earthquake: fault constraints provided by multiple SAR techniques, *Geophys. J. Int.,* **195**(1), 650–660.

Fialko, Y. 2004. Probing the mechanical properties of seismically active crust with space geodesy: study of the coseismic deformation due to the 1992 Mw7.3 Landers (southern California) earthquake, *J. geophys. Res.,* **109**(B3), doi:10.1029/2003JB002756.

Fialko, Y., Sandwell, D., Rosen, P.A., Simons, M. & Khazan, Y. 2002. Deformation on nearby faults induced by the 1999 Hector Mine Earthquake, *Science,* **297**(5586), 1858–1862.

Fialko, Y., Sandwell, D., Simons, M., Avouac, J.P. & Leyder, C. 2005. Three-dimensional deformation caused by the Bam, Iran, earthquake and the origin of shallow slip deficit, *Nature,* **435**(7040), 295–299.

Fialko, Y., Simons, M. & Agnew, D. 2001. The complete (3-D) surface displacement field in the epicentral area of the 1999 Mw 7.1 Hector Mine Earthquake, California, from space geodetic observations, *Geophys. Res. Lett.,* **28**(16), 3063–3066.

Freed, A.M., Bürgmann, R., Calais, E. & Freymueller, J. 2006. Stress-dependent power-law flow in the upper mantle following the 2002 Denali, Alaska, earthquake, *Earth planet. Sci. Lett.,* **252**(3–4), 481–489.

Freymuller, J.T., Feigl, K.L. & Rabaute, T. 1993. The displacement field of the Landers earthquake mapped by radar interferometry, *Nature,* **364**, 138–142.

Goldstein, R. & Werner, C. 1998. Radar interferogram filtering for geophysical applications, *Geophys. Res. Lett.,* **25**(22), 4035–4038.

Guilbaud, C., Simoes, M., Barrier, L., Laborde, A., Van der Woerd, J., Li, H. & Murray, A. 2017. Kinematics of active deformation across the Western Kunlun mountain range (Xinjiang, China) and potential seismic hazards within the southern Tarim Basin, *J. geophys. Res.,* **122**(11), 10 398–10 426.

Gunawan, E. et al. 2014. A comprehensive model of post-seismic deformation of the 2004 Sumatra-Andaman earthquake deduced from GPS observations in northern Sumatra, *J. Asian Earth Sci.,* **88**, 218–229.

Guo, Z., Motagh, M., Hu, J.-C., Xu, G., Haghighi, M.H., Bahroudi, A., Fathian, A. & Li, S. 2022. Depth-varying friction on a ramp-flat fault illuminated by ∼3-year InSAR observations following the 2017 Mw 7.3 Sarpol-e Zahab earthquake, *J. geophys. Res.,* **127**, e2022JB025148.

Harris, R.A., 1998. Introduction to special section: stress triggers, stress shadows, and implications for seismic Hazard, *J. geophys. Res.,* **103**, 24 347–24 358.

He, K., Wen, Y., Xu, C. & Zhao, Y. 2022. Fault geometry and slip distribution of the 2021 Mw 7.4 Maduo, China, Earthquake inferred from InSAR measurements and relocated aftershocks, *Seismol. Res. Lett.,* **93**(1), 8–20.

He, P., Wang, Q., Ding, K., Li, J. & Zou, R. 2016. Coseismic and postseismic slip ruptures for 2015 Mw 6.4 Pishan earthquake constrained by static GPS solutions, *Geod. Geodyn.,* **7**(5), 323–328

Hersbach, H. et al. 2020. The ERA5 global reanalysis. *Q. J. R. Meteor. Soc.,* **146**(730), 1999–2049.

Huang, H., Xu, W.B., Meng, L.S., Bürgmann, R. & Baez, J.C. 2017. Early aftershocks and afterslip surrounding the 2015 Mw 8.4 Illapel rupture, *Earth planet. Sci. Lett.,* **457**, 282–291.

Huang, M.-H., Bürgmann, R. & Pollitz, F. 2016. Lithospheric rheology constrained from twenty-five years of post-seismic deformation following the 1989 Mw6.9 Loma Prieta earthquake, *Earth planet. Sci. Lett.,* **435**, 147–158.

Huang, M.H., Bürgmann, R. & Freed, A. 2014. Probing the lithospheric rheology across the eastern margin of the Tibetan Plateau, *Earth planet. Sci. Lett,* **396**, 88–96.

Jiang, X. & Li, Z. 2014. Seismic reflection data support episodic and simultaneous growth of the Tibetan plateau since 25 Myr, *Nat. Commun.,* **5**, 5453.

Jin, Z., Fialko, Y., Yang, H. & Li, Y. 2023. Transient deformation excited by the 2021 M7.4 Maduo (China) earthquake: evidence of a deep shear zone, *J. geophys. Res.,* **128**, e2023JB026643.

Jin, Z., Fialko, Y., Zubovich, A. & Schöne, T. 2022. Lithospheric deformation due to the 2015 M7.2 Sarez (Pamir) earthquake constrained by 5 years of space geodetic observations, *J. geophys. Res.,* **127**, e2021JB022461.

Jónsson, S., Segall, P., Pedersen, R. & Björnsson, G. 2003. Post-seismic ground movements correlated to pore-pressure transients, *Nature,* **424**(6945), 179–183.

Jónsson, S., Zebker, H., Segall, P. & Amelung, F. 2002. Fault slip distribution of the 1999 Mw 7.1 hector mine, California, earthquake, estimated from satellite radar and GPS measurements, *Bull. seism. Soc. Am.,* **92**(4), 1377–1389.

Kao, H., Gao, R., Rau, R.-J., Shi, D., Chen, R.-Y., Guan, Y. & Wu, F.T.(2001. Seismic image of the Tarim basin and its collision with, *Tibet. Geology,* **29**(7), 575–578.

Koch, K.R. & Kusche, J. 2002. Regularization of geopotential determination from satellite data by variance components, *J. Geod.,* **76**, 259–268.

Laske, G., Masters, G., Ma, Z. & Pasyanos, M. 2013. Update on CRUST1.0—a 1-degree global model of Earth's crust, in *Proceedings of the EGU General Assembly,* Vienna, Austria.

Li, H.B., Woerd, J.V., Sun, Z.M., Si, L., Tapponnier, P., Pan, J.W. & Liu, D.L. 2012. Co-seismic and cumulative offsets of the recent earthquakes along the Karakax left-lateral strike-slip fault in western Tibet, *Gondwana Res.,* **21**, 64–87.

Li, K., Li, Y., Tapponnier, P., Xu, X., Li, D. & He, Z. 2022. Joint In-SAR and field constraints on faulting during the Mw 6.4, July 23, 2020, Nima/Rongma Earthquake in Central Tibet, *J. geophys. Res.,* **126**, e2021JB022212.

Li, Q.S. et al. 2002. Tarim underthrust beneath western Kunlun: evidence from wide-angle seismic sounding, *J. Asian Earth Sci.,* **20**(3), 247–253.

Li, T., Chen, J., Fang, L., Chen, Z., Thompson, J.A. & Jia, C. 2016. The 2015 Mw 6.4 Pishan earthquake: seismic hazards of an active blind wedge thrust system at the Western Kunlun Range Front Northwest Tibetan Plateau, *Seismol. Res. Lett.,* **87**(3), 601–608.

Li, Z.C., et al. 2009. Wenchuan earthquake deformation fault inversion and analysis based on GPS observation, *Acta Geod. Cartograph. Sin.,* **38**(2), 108–113 +119 (in Chinese with English abstract).

Lin, A.M., Ren, Z.K., Jia, D. & Wu, X. 2009. Co-seismic thrusting rupture and slip distribution produced by the 2008 Mw 7.9 Wenchuan earthquake, China, *Tectonophysics,* **471**(3-4), 203–215.

Lin, C.S., Yang, H.J. & Liu, J.Y. 2012. Distribution and erosion of the Paleozoic tectonic unconformities in the Tarim Basin, Northwest China: significance for the evolution of paleo-uplifts and tectonic geography during deformation, *J. Asian Earth Sci.,* **46**, 150–160.

Linde, A.T. & Johnston, M.J.S. 1989. Source parameters of the October 1, 1987 Whittier narrows earthquake from crustal deformation data, *J. geophys. Res.,* **94**(B7), 9633–9643.

Liu, Z.J. et al.(2009). Co-seismic ruptures of the 12 May 2008, Ms 8.0 Wenchuan earthquake, Sichuan: east–west crustal shortening on oblique, parallel thrusts along the eastern edge of Tibet, *Earth planet. Sci. Lett.,* **286**(3-4), 355–370.

Lu, R., Xu, X., He, D., Liu, B., Tan, X. & Wang, X. 2016. Coseismic and blind fault of the 2015 Pishan Mw 6.5 earthquake: implications for the sedimentary-tectonic framework of the western Kunlun Mountains, northern Tibetan Plateau, *Tectonics,* **35**, 956–964.

Marone, C. 1998. The effect of loading rate on static friction and the rate of fault healing during the earthquake cycle, *Tectonophysics,* **295**(1-2), 127–139.

Massonnet, D., Rossi, M., Carmona, C., Adragna, F., Peltzer, G., Feigl, K., Rabaute, T. & Viotto, P. 1993. The displacement field of the Landers earthquake mapped by radar interferometry, *Nature,* **364**(6433), 138–142.

Matte, P. et al. 1996. Tectonics of western Tibet, between the Tarim and the Indus, *Earth planet. Sci. Lett.,* **142**(3-4), 311–330.

Nur, A. 1972. Aftershocks caused by pore fluid flow? *Science,* **175**(4024), 885–887.

Okada, Y. 1985. Surface deformation to shear and tensile faults in a half-space, *Bull. seism. Soc. Am.,* **75**(4), 1135–1154.

Pei, J.L., Li, H.B., Si, J.L., Pan, J.W., Wu, F.Y., Sun, Z.M. & Zhao, Y. 2011. The response of the Tibet uplift since Lower Pleistocene in the center of Tarim Basin [in Chinese with English abstract], *Acta Petrol. Sin.,* **27**(11), 3487–3498.

Peltzer, G. 1999. Evidence of nonlinear elasticity of the crust from the Mw7.6 Manyi (Tibet) earthquake, *Science,* **286**(5438), 272–276.

Peltzer, G., Rosen, P., Rogez, F., Hudnut, K. & Funning, G. 1996. Post-seismic rebound in fault step-overs caused by pore fluid flow, *Science,* **273**(5279), 1202–1204.

Pollitz, F.F. 2019. Lithosphere and shallow asthenosphere rheology from observations of post-earthquake relaxation, *Phys. Earth planet. Inter.,* **293**, 106271, doi:10.1016/j.pepi.2019.106271.

Reasenberg, P.A. & Simpson, R.W., 1992. Response of regional seismicity to the static stress change produced by the Loma Prieta earthquake. *Science,* **255**, 1687–1690.

Rosen, P.A. et al. 2018. The insar scientific computing environment 3.0: a flexible framework for nisar operational and user-led science processing, in *IGARSS 2018-2018 IEEE International Geoscience and Remote Sensing Symposium,* IEEE, pp. 4897–4900.

Rousset, B., Barbot, S., Avouac, J.P. & Hsu, Y.J. 2012. Postseismic deformation following the 1999 Chi—Chi earthquake, Taiwan: implication for lower—crust rheology, *J. geophys. Res.,* **117**(B12), doi:10.1029/2012JB009571.

Sabadini, R. & Vermeersen, B.L.A. 2004. Normal mode theory in viscoelasticity, in *Global Dynamics of the Earth: Applications of Normal Mode Relaxation Theory to Solid-Earth Geophysics,* pp. 1–44, Kluwer Academic Publishers.

Sandwell, D.T., Myer, D., Mellors, R., Sichoix, L. & Nandakumar, K. 2008. Accuracy and resolution of ALOS interferometry: vector deformation maps of the Father's Day intrusion at Kilauea, *IEEE Trans. Geosci. Remote Sens.,* **46**(11), 3524–3534.

Schwintzer, P. 1990. Sensitivity analysis in least squares gravity modeling by means of redundancy decomposition of stochastic prior information, Internal Report, Deutsches Geodatisches Forschungsinstitut.

Shen, Z.K. et al. 2009. Slip maxima at fault junctions and rupturing of barriers during the 2008 Wenchuan earthquake, *Nat. Geosci.,* **2**(10), 718–724.

Si, J.L., Li, H.B., Pei, J.L., Sun, Z.M., Pan, J.W. & Qiu, Z.L. 2011. Sedimentary environment variation and its tectonic significance of Mazar Tagh in the middle Tarim Basin [in Chinese with English abstract], *Acta Petrol. Sin.,* **27**(1), 321–332.

Sobel, E. & Dumitru, T. 1997. Thrusting and exhumation around the margins of the western Tarim basin during the India-Asia collision, *J. geophys. Res.,* **102**, 5043–5063.

Sudhaus, H. & Jónsson, S. 2009. Improved source modelling through combined use of InSAR and GPS under consideration of correlated data errors: application to the June 2000 Kleifarvatn earthquake, Iceland, *Tectonophysics,* **474**(2), 69–77.

Sun, J., Shen, Z.-K., Li, T. & Chen, J. 2016. Thrust faulting and 3D ground deformation of the 3 July 2015 Mw 6.4 Pishan, China earthquake from Sentinel-1A radar interferometry, *Tectonophysics,* **683**, 77–85.

Tikhonov, A.N. 1963a. Regularization of ill-posed problems, *Dokl. Akad. Nauk SSSR,* **151**(1), 49–52.

Tikhonov, A.N. 1963b. Solution of incorrectly formulated problems and the regularization method, *Dokl. Akad. Nauk SSSR,* **151**(3), 501–504.

Wang, C.Y., Chen, H.L., Cheng, X.G. & Li, K. 2013. Evaluating the role of syn-thrusting sedimentation and interaction with frictional detachment in the structural evolution of the SW Tarim Basin, NW China: insights from analogue modeling, *Tectonophysics,* **608**, 642–652.

Wang, L.Y., Zhao, X. & Gao, H. 2018a. A method for determining the regularization parameter and the relative weight ratios of the seismic slip distribution with multi-source data, *J. Geodyn.,* **118**(7), 1–10.

Wang, L.Y., Zhao, X., Xu, W.B., Xie, L. & Fang, N. 2019. Coseismic slip distribution inversion with unequal weighted Laplacian smoothness constraints, *Geophys. J. Int.,* **218**, 145–162.

Wang, R.J., Francisco, L.M. & Roth, F. 2006. PSGRN/PSCMP—a new code for calculating co- and post-seismic deformation, geoid and gravity changes based on the viscoelastic-gravitational dislocation theory, *Comput. Geosci.,* **32**(4), 527–541.

Wang, S., Zhang, Y., Wang, Y., Jiao, J., Ji, Z. & Han, M. 2020. Postseismic deformation mechanism of the July 2015 MW 6.5 Pishan earthquake revealed by Sentinel-1A InSAR observation, *Sci. Rep.,* **10**, 18536.

Wang, X., Wang, W., Zhao, J. & Yao, Z. 2018b. Rupture process of the 2015 Pishan earthquake from joint inversion of InSAR, teleseismic data and GPS, *Sci. China Earth Sci.,* **61,** 1467–1481.

Wen, Y., Xu, C., Liu, Y. & Jiang, G., 2016.Deformation and Source Parameters of the 2015 Mw 6.5 Earthquake in Pishan, Western China, from Sentinel-1A and ALOS-2 Data. *Remote Sens.,* **8**(2), 134. doi: 10.3390/rs8020134.

Wright, T.J., Lu, Z. & Wicks, C. 2003. Source model for the Mw 6.7, 23 October 2002, Nenana Mountain Earth-quake (Alaska) from InSAR, *Geophys. Res. Lett.,* **30**(18), doi:10.1029/2003GL018014.

Xu, C.J., Ding, K.H., Cai, J.Q. & Grafarend, E.W. 2009. Methods of determining weight scaling factors for geodetic-geophysical joint inversion, *J. Geodyn.,* **47**(1), 39–46.

Xu, Z.Q., Li, S.T., Zhang, J.X., Yang, J.S., He, B.Z. & Li, H.B. 2011. Paleo-Asian and Tethyan tectonic systems with docking the Tarim block [in Chinese with English abstract], *Acta Petrol. Sin.,* **36**(1), 1–22.

Yin, A. *et al.* 2002. Tectonic history of the Altyn Tagh fault system in northern Tibet inferred from Cenozoic sedimentation, *Geol. Soc. Am. Bull.,* **114,** 1257–1295.

Zhang, G., Qu, C., Shan, X., Song, X., Zhang, G., Wang, C., Hu, J.-C. & Wang, R. 2011. Slip distribution of the 2008 Wenchuan Ms7.9 earthquake by joint inversion from GPS and InSAR measurements: a resolution test study, *Geophys. J. Int.,* **186**(1), 207–220.

Zhang, Y.A., Fattahi, H. & Amelung, F. 2019. Small baseline InSAR time series analysis: unwrapping error correction and noise reduction, *Comput. Geosci.,* **133,** doi:10.1016/j.cageo.2019.104331.

Zhao, X., Xu, C., Wen, Y., He, K., Y, J. & Wang, J. 2023. Early post-seismic deformation of the 2017 Mw 7.3 Darbandikhan, Iran/Iraq Earthquake on a flat-ramp-flat fault, *Tectonophysics,* **853,** doi:10.1016/j.tecto.2023.229809.

Zhao, X., Xu, C., Zhou, L., Wen, Y., Wang, J. & Zhao, Y. 2022. A new method applied for the determination of relative weight ratios under the TensorFlow platform when estimating coseismic slip distribution, *J. geophys. Res.,* **127,** e2022JB024843.

Zheng, G. *et al.* 2017. Crustal deformation in the India-Eurasia collision zone from 25 years of GPS measurements, *J. geophys. Res.,* **122,** 9290–9312.